Co-optimization of SnS absorber and Zn(O,S) buffer materials for improved solar cells

Citation	Park, Helen Hejin, Rachel Heasley, Leizhi Sun, Vera Steinmann, Rafael Jaramillo, Katy Hartman, Rupak Chakraborty, Prasert Sinsermsuksakul, Danny Chua, Tonio Buonassisi, Royb G. Gordon, (2015), Co-optimization of SnS absorber and Zn(O,S) buffer materials for improved solar cells. Progress in Photovoltaics 23 (7): 901–908.
Published Version	doi:10.1002/pip.2504
Accessed	October 12, 2017 8:45:26 AM EDT
Citable Link	http://nrs.harvard.edu/urn-3:HUL.InstRepos:12311539
Terms of Use	This article was downloaded from Harvard University's DASH repository, and is made available under the terms and conditions applicable to Open Access Policy Articles, as set forth at http://nrs.harvard.edu/urn-3:HUL.InstRepos:dash.current.terms-of-use#OAP

Co-optimization of SnS Absorber and Zn(O,S) Buffer Materials for Improved Solar Cells

Helen Hejin Park,[1] Rachel Heasley,[1] Leizhi Sun,[1] Vera Steinmann,[2] R. Jaramillo,[2]
Katy Hartman,[2] Rupak Chakraborty,[2] Prasert Sinsermsuksakul,[1] Danny Chua,[1]
Tonio Buonassisi,[2] and Roy G. Gordon[1,*]
[1]*Harvard University, Cambridge, Massachusetts 02138, USA*
[2]*Massachusetts Institute of Technology, Cambridge, Massachusetts 02139, USA*

Thin-film solar cells consisting of earth-abundant and non-toxic materials were made from pulsed chemical vapor deposition (pulsed-CVD) of SnS as the *p*-type absorber layer and atomic layer deposition (ALD) of Zn(O,S) as the *n*-type buffer layer. The effects of deposition temperature and annealing conditions of the SnS absorber layer were studied for solar cells with a structure of Mo/SnS/Zn(O,S)/ZnO/ITO. Solar cells were further optimized by varying the stoichiometry of Zn(O,S) and the annealing conditions of SnS. Post-deposition annealing in pure hydrogen sulfide improved crystallinity and increased the carrier mobility by one order of magnitude, and a power conversion efficiency up to 2.9% was achieved.

Keywords: SnS thin-film solar cell, Zinc Oxysulfide, Buffer Layer, Atomic Layer Deposition, Pulsed-Chemical Vapor Deposition

---

[*] **Email: gordon@chemistry.harvard.edu Phone: +1-617-495-4017 Fax: +1-617-495-4723**

Introduction

Tin monosulfide (SnS) has shown to be a promising alternative *p*-type absorber material to conventional $Cu(In,Ga)(S,Se)_2$ (CIGS) and CdTe due to its earth-abundancy and non-toxicity, suitable bandgap of 1.1 – 1.5 eV [1,2], and high absorption coefficient above 10^4 cm^{-1} [3,4]. Furthermore, SnS is a binary compound that involves simpler growth chemistry compared to $Cu_2ZnSn(Se,S)_4$ [5,6], another investigated earth-abundant absorber material. Zinc oxysulfide, Zn(O,S), has shown to be a promising non-toxic *n*-type buffer layer to replace the conventional toxic CdS [7,8] in CIGS-based solar cells [8]. Zn(O,S) allows simple tuning of the conduction band offset (CBO) at the *p*-*n* junction interface by optimizing the oxygen and sulfur contents of Zn(O,S) [9-11], which can be easily done with atomic layer deposition (ALD) by altering the number of pulses for each precursor [7,12,13]. Such tunability of the buffer layer is important, since a “cliff” structure in the conduction-band energy alignment ($E_{c,absorber} > E_{c,buffer}$) increases interface recombination, whereas a “spike” structure ($E_{c,absorber} < E_{c,buffer}$) forms a barrier that blocks photocurrent collection for CBO larger than 0.5 eV [8,14-19]. Recently, heterojunction solar cells using a *p*-type SnS absorber layer and an *n*-type ZnO-based buffer layer have shown to be a promising path towards earth-abundant non-toxic thin-film solar cells exhibiting a certified total-area record efficiency of 2.04% (uncertified active-area efficiency of 2.46%) with Zn(O,S) buffer layers [9], and an efficiency of 2.1% with $Zn_{1-x}Mg_xO$ buffer layers [20]. Although SnS exhibits properties suitable for an absorber layer, grain boundaries and defects such as sulfur vacancies in the bulk can induce recombination centers, which diminish the performance of the solar cells [21]. Such defects can be reduced or eliminated by providing sulfur to the film through an appropriate post-annealing atmosphere.

In this paper, we grow SnS by pulsed-chemical vapor deposition (pulsed-CVD) from a cyclic tin(II) amide precursor [22] and improve its quality by varying the temperatures of growth and post-deposition annealing. The device performance was further improved by optimizing the oxygen and sulfur contents of the Zn(O,S) buffer layer. Since different growth and annealing conditions of SnS can change the conduction-band energy level of the absorber layer, tuning of the CBO through the Zn(O,S) buffer layer composition is critical to optimizing the band alignment across the junction [23]. For the optimum conditions, the solar cell efficiency reaches 2.9%, the highest yet reported for solar cells with SnS as the absorber layer.

Experimental Procedure

Solar cell devices with a structure of Si/SiO_2/Mo/SnS/Zn(O,S)/ZnO/ITO/Ag were fabricated. A schematic diagram of the device stack is shown in Figure 1(a). A bilayer of Mo (1 μm, 0.3 ohm/sq) was sputtered onto silicon (100) substrates with about 300 nm of silicon dioxide on top. The first layer of Mo was sputtered for 30 min at a working pressure of 10 mTorr, and the second layer for 30 min at 2 mTorr [24].

A pulsed-CVD process was used to grow ~500 nm of SnS using N^2,N^3-di-tert-butyl-butane-2,3-diamido-tin(II) ($C_{12}H_{26}N_2Sn$, Sigma Aldrich) and 4% H_2S in N_2 for the Sn and S precursors, respectively. The structure of the Sn precursor is shown in Figure 1(b). SnS films were grown at either 70°C or 120°C, and the Sn precursor source was kept at 40°C. Each pulsed-CVD cycle consisted of a dose of the Sn precursor with N_2 assistance for 1 s, then a dose of H_2S to mix and react with the Sn precursor in the deposition zone for 1 s in closed valve mode, and then evacuation for 2 s. The pressures for the Sn precursor, N_2 assist, and H_2S were 3.7, 152.4 and 154.5 Torr, respectively. The volumes of the vapor space used for dosing each precursor were approximately 13.6, 29.9, and 10.7 mL for the Sn precursor, N_2 assist, and H_2S, respectively and were all kept at 40°C. Based on these values, the exposure of each dose of Sn precursor, N_2 assist, and H_2S were approximately 0.20, 18, and 6.50 Torr·s, respectively. SnS films were annealed in pure H_2S (constant flow) with a vapor pressure of ~6.5 Torr for 1.5 h at temperatures of 200°C, 300°C, and 400°C. Based on the phase diagram of SnS and previous studies [25,26], SnS is known to evaporate congruently, and stoichiometry of the films should remain the same for the annealing temperatures investigated in this study.

Zn(O,S) (30 nm) and ZnO (10 nm) were grown at 120°C by ALD. Diethylzinc (DEZ, $Zn(C_2H_5)_2$, Strem Chemicals), deionized H_2O, and a gas mixture of 4% H_2S in N_2 were used as the zinc, oxygen, and sulfur sources at room temperature, respectively. The pressures for the Zn precursor, H_2O, and H_2S were 7.5, 7.8, and 154.5 Torr, respectively. The exposures used for each dose of DEZ, H_2O, and H_2S are estimated to be approximately 0.13, 0.15, and 6.50 Torr·s with trapped volumes of 4.4, 4.8, and 10.7 mL, respectively, which were all kept at 40°C. Each precursor was exposed to the substrate for 1 s using closed valve mode. The purge times for each precursor were 30, 30, and 10 s for DEZ, H_2O, and H_2S, respectively. The ALD sequence for Zn(O,S) was $(DEZ/N_2/H_2O/N_2) \times m + (DEZ/N_2/H_2S/N_2) \times n$, where m and n indicate the number of pulses for ZnO and ZnS, respectively. Stoichiometry of the Zn(O,S) films was measured by Rutherford backscattering spectroscopy (RBS). By RF magnetron sputtering, 200 nm of indium tin oxide (ITO) was deposited at room temperature through a shadow mask to define the device area (0.25 cm^2). For the top electrode, 500 nm of Ag was electron-beam evaporated through a shadow mask at room temperature.

Current density vs. voltage (*J*-*V*) characteristics were measured with a Keithley 4200 sourcemeter. The standard 100 mW/cm^2 (1 Sun) illumination was generated by a Newport Oriel 91194 solar simulator with a 1300 W Xe-lamp using an AM1.5G filter, and a Newport Oriel

68951 flux controller calibrated by an NREL-certified Si reference cell equipped with a BK-7 window. External quantum efficiency (EQE) measurements were performed with a PV Measurements Model QEX7 tool at room temperature.

Van der Pauw measurements and Hall effect were used to determine the carrier concentration and carrier type of individual layers. The carrier mobility was then determined from $\rho = 1/pe\mu$, where ρ is the resistivity, p is the carrier concentration, e is the electron charge, and μ is the carrier mobility. Cross-sectional (with 12° tilt) and plan-view morphology of SnS films were examined by field-emission scanning electron microscopy (FESEM, Zeiss, Ultra-55). The crystal structure and texture of the films were analyzed by x-ray diffraction (XRD, PANalytical X-Pert Pro) with Cu $K\alpha$ radiation using a θ-2θ scan. SnS films were grown on quartz substrates for Hall measurements, on a layered substrate of Si/SiO_2/Mo for XRD analysis, on glassy carbon substrates for RBS, and on Si(100) substrates for FESEM.

Results and Discussion

The dependence of H_2S annealing temperature on the electrical properties of SnS were investigated. Figure 2 compares SnS films grown at 70°C (dotted) and 120°C (solid). Resistivity of the films tended to decrease with increasing annealing temperature, and hole carrier concentrations ranged from 10^{15} to 10^{16} cm^{-3} for both depositions temperatures. The hole mobility increased with the H_2S annealing temperatures due to the decrease in resistivity. Raising the deposition temperature from 70°C to 120°C improved the mobility of the as-deposited SnS film from 1 to 4 $cm^2/V\cdot s$. The mobility of the as-deposited film grown at 120°C is comparable to the film grown at 70°C and annealed at 300°C. Annealing films grown at 120°C, improved the mobility from 4 to 10 $cm^2/V\cdot s$. The enhanced mobility could be due to the improvement of crystallinity (point and extended defects). Grain growth from annealing is observed in the cross-sectional and plan-view SEM images shown in Figure 3. Much larger grain growth after H_2S annealing was observed for the higher deposition temperature. This is because the grains of the as-deposited film grown at 120°C start off larger than those grown at 70°C. Raising the deposition temperature to 120°C also eliminated pinholes that were observed to increase in number with annealing temperature for films deposited at 70°C.

For SnS films grown at 120°C, the effect of H_2S annealing temperature on the solar-cell performance was investigated for a fixed Zn(O,S) buffer layer with S/Zn = 0.37, as determined by RBS. Figure 4 shows *J-V* plots under dark and 1 Sun illumination. Compared to the device with as-deposited SnS, the devices with SnS annealed in pure H_2S resulted in larger short-circuit current densities (J_{SC}) and open-circuit voltages (V_{OC}) due to the improvement of the SnS absorber layer quality. The improvement in V_{OC} can be explained by the overall tendency shown in the dark saturation current, whereas the improvement in J_{SC} can be explained by the improved carrier collection (Fig. 7a). The device with SnS annealed at 300°C showed a cell performance of J_{SC} = 17.9 mA/cm^2, V_{OC} = 256 mV, *FF* = 42.0%, and η = 1.9%, and the device with SnS annealed at 400°C showed a cell performance of J_{SC} = 18.5 mA/cm^2, V_{OC} = 235 mV, *FF* = 42.8%, and η = 1.9%, as summarized in Table 1. The device with SnS annealed at 300°C showed improvement with less leakage current compared to the device with as-deposited SnS. However, the leakage current increased when annealing SnS at 400°C in pure H_2S, resulting in lower V_{OC}.

For devices with SnS annealed in H_2S at 300°C and 400°C, different stoichiometries of Zn(O,S) were investigated to further improve the band alignment of the solar cell, as shown in the *J-V* characteristics under dark and 1 Sun illumination in Figure 5. For both SnS annealing temperatures, higher sulfur content in Zn(O,S) led to lower current leakage. For the devices with SnS annealed at 300°C, as the sulfur content in Zn(O,S) increased, the J_{SC} decreased and the V_{OC}

increased due to the increase in the conduction band energy level of Zn(O,S) [23]. For Zn(O,S) with S/Zn = 0.50, the device performance improved with J_{SC} = 14.1 mA/cm^2, V_{OC} = 305 mV, and FF = 53.1%, as summarized in Table 2. The efficiency increased to η = 2.3%, due to the improvement in V_{OC} and FF. However, for Zn(O,S) with S/Zn > 0.50, the device performance significantly deteriorated because the conduction band energy level of Zn(O,S) was too high, impeding the photo-generated electron flow, and resulting in very low J_{SC} and poor FF. For the devices with SnS annealed at 400°C and Zn(O,S) with S/Zn = 0.14, the rectifying behavior was lost due to the high conductivity of the buffer layer. For the devices with SnS annealed at 400°C and Zn(O,S) with S/Zn > 0.14, the J_{SC} increased with decreasing sulfur content in the buffer layer. The solar cell performance improved to J_{SC} = 24.9 mA/cm^2, V_{OC} = 261 mV, FF = 44.4%, and η = 2.9% for Zn(O,S) with S/Zn = 0.26 and SnS annealed at 400°C. For the devices with SnS annealed at 300°C and 400°C, the optimum Zn(O,S) S/Zn ratios were 0.50 and 0.26, respectively. This variation in optimum Zn(O,S) sulfur content is probably due to the change in surface conduction-band position of SnS from the different annealing conditions, leading to different CBO at the SnS/Zn(O,S) interface.

Figure 6 shows the XRD scans of as-deposited SnS grown at 70°C, and as-deposited and H_2S annealed SnS films grown at 120°C. The as-deposited films mainly have the cubic structure (JCPDS No. 04-004-8426) that is reported to be stable at low temperatures [27]. After annealing, the films convert to the orthorhombic phase (JCPDS No. 00-039-0354) that is stable at higher temperatures [28]. The orthorhombic (111) peak of SnS decreases as the deposition temperature increases from 70°C to 120°C. For films grown at 120°C, the orthorhombic (111) peak increases with H_2S annealing, and the orthorhombic (021) peak increases with increasing annealing temperature. Such change in crystal orientation from the different annealing temperatures is probably why the surface conduction-band position of SnS changes [29-31], resulting in variation of the optimum Zn(O,S) sulfur content for the solar cell devices [9].

External quantum efficiency measurements can be found in Figure 7. For devices with increasing annealing temperature of SnS, EQE near the high wavelength region ($\lambda > 600$ nm) increased significantly, whereas EQE near the low wavelength region ($\lambda < 450$ nm) remained approximately the same. The EQE enhancement at high wavelengths indicates collection-length improvement with H_2S annealing of SnS. Crystallinity improvement could be a possible reason for the improvement in collection length as shown by the increased red light response. For devices with SnS annealed at 400°C, EQE remained similar in the low wavelength region ($\lambda < 450$ nm) despite the different sulfur contents in Zn(O,S), which is probably because Zn(O,S) is only 30 nm thick, allowing the ITO layer to do most of the absorbing for the low-wavelength region. The overall EQE increased with decreasing sulfur content in Zn(O,S), which agrees well with the *J-V* characteristics under illumination.

Conclusions

Devices with efficiencies up to 2.9% were achieved through improvement of the SnS absorber layer quality *via* annealing and varying the stoichiometry of Zn(O,S). We successfully demonstrated solar-cell device improvements through annealing the SnS absorber layer in pure H_2S, which improves crystallinity and reduces the density of grain boundaries. Different deposition and annealing temperatures can lead to variations of the surface conduction-band positions of SnS, which is why it is beneficial to use a buffer layer with variable compositions like Zn(O,S) so that the CBO at the *p-n* junction interface can be easily optimized.

Acknowledgements

The authors thank Dr. Daniel Moser of Sigma-Aldrich for providing the Sn precursor. This work was supported by the U.S. Department of Energy (DE-EE0005329). K. Hartman and R. Jaramillo acknowledge the support of an Intel PhD Fellowship and a DOE EERE Postdoctoral Research Award, respectively. Part of the work was performed at the Center of Nanoscale Systems (CNS) at Harvard University, a member of the National Nanotechnology Infrastructure Network (NNIN), which is supported by NSF (ECS-0335765).

References

[1] Hartman K, Johnson JL, Bertoni MI, Recht D, Aziz MJ, Scarpulla MA, Buonassisi T. SnS thin-films by RF sputtering at room temperature. *Thin Solid Films* 2011; **519**: 7421-7424. DOI: 10.1016/j.tsf.2010.12.186

[2] Reddy KTR, Reddy NK, Miles RW. Photovoltaic properties of SnS based solar cells. *Solar Energy Materials and Solar Cells* 2006; **90**: 3041-3046. DOI: 10.1016/j.solmat.2006.06.012

[3] Reddy NK, Hahn YB, Devika M, Sumana HR, Gunasekhar KR. Temperature-dependent structural and optical properties of SnS films. *Journal of Applied Physics* 2007; **101**: 093522. DOI: 10.1063/1.2729450

[4] Noguchi H, Setiyadi A, Tanamura H, Nagatomo T, Omoto O. Characterization of Vacuum-evaporated tin sulfide film for solar-cell materials. *Solar Energy Materials and Solar Cells* 1994; **35**: 325-331. DOI: 10.1016/0927-0248(94)90158-9

[5] Shin B, Gunawan O, Zhu Y, Bojarczuk NA, Chey SJ, Guha S. Thin film solar cell with 8.4% power conversion efficiency using an earth-abundant Cu_2ZnSnS_4 absorber. *Progress in Photovoltaics*: *Research and Applications* 2013; **21**: 72-76. DOI: 10.1002/Pip.1174

[6] Todorov TK, Reuter KB, Mitzi DB. High-efficiency solar cell with earth-abundant liquid-processed absorber. *Advanced Energy Materials* 2010; **22**: E156-E159. DOI: 10.1002/adma.200904155

[7] Sanders BW, Kitai A. Zinc oxysulfide thin-films grown by atomic layer deposition. *Chemistry of Materials* 1992; **4**: 1005-1011. DOI: 10.1021/Cm00023a015

[8] Merdes S, Saez-Araoz R, Ennaoui A, Klaer J, Lux-Steiner MC, Klenk R. Recombination mechanisms in highly efficient thin film Zn(S,O)/Cu(In,Ga)S_2 based solar cells. *Applied Physics Letters* 2009; **95**: 213502. DOI: 10.1063/1.3266829

[9] Sinsermsuksakul P, Hartman K, Kim SB, Heo J, Sun LZ, Park HH, Chakraborty R, Buonassisi T, Gordon RG. Enhancing the efficiency of SnS solar cells via band-offset engineering with a zinc oxysulfide buffer layer. *Applied Physics Letters* 2013; **102**: 053901. DOI: 10.1063/1.4789855

[10] Platzer-Bjorkman C, Torndahl T, Abou-Ras D, Malmstrom J, Kessler J, Stolt L. Zn(O,S) buffer layers by atomic layer deposition in Cu(In,Ga)Se_2 based thin film solar cells: band alignment and sulfur gradient. *Journal of Applied Physics* 2006; **100**: 044506. DOI: 10.1063/1.2222067

[11] Persson C, Platzer-Bjorkman C, Malmstrom J, Torndahl T, Edoff M. Strong valence-band offset bowing of $ZnO_{1-x}S_x$ enhances p-type nitrogen doping of ZnO-like alloys. *Physical Review Letters* 2006; **97**: 146403. DOI: 10.1103/Physrevlett.97.146403

[12] Park HH, Heasley R, Gordon RG. Atomic layer deposition of Zn(O,S) thin films with tunable electrical properties by oxygen annealing. *Applied Physics Letters* 2013; **102**: 132110. DOI: 10.1063/1.4800928

[13] Bakke JR, Tanskanen JT, Hagglund C, Pakkanen TA, Bent SF. Growth characteristics, material properties, and optical properties of zinc oxysulfide films deposited by atomic layer deposition. *Journal of Vacuum Science & Technology A* 2012; **30**: 01A135. DOI: 10.1116/1.3664758

[14] Choi H, Kim J, Nahm C, Kim C, Nam S, Kang J, Lee B, Hwang T, Kang S, Choi DJ, Kim Y, Park B. The role of ZnO-coating-layer thickness on the recombination in CdS quantum-dot-sensitized solar cells. *Nano Energy* 2013; **2**: 1218. DOI: 10.1016/j.nanoen.2013.05.007

[15] Kim J, Choi H, Nahm C, Moon J, Kim C, Nam S, Jung D, Park B. The effect of a blocking layer on the photovoltaic performance in CdS quantum-dot-sensitized solar cells. *Journal of Power Sources* 2011; **196**: 10526-10531. DOI: 10.1016/j.jpowsour.2011.08.052

[16] Minemoto T, Matsui T, Takakura H, Hamakawa Y, Negami T, Hashimoto Y, Uenoyama T, Kitagawa M. Theoretical analysis of the effect of conduction band offset of window/CIS layers on performance of CIS solar cells using device simulation. *Solar Energy Materials and Solar Cells* 2001; **67**: 83-88. DOI: 10.1016/S0927-0248(00)00266-X

[17] Niemegeers A, Burgelman M, Devos A. On the CdS/CuInSe$_2$ conduction-band discontinuity. *Applied Physics Letters* 1995; **67**: 843-845. DOI: 10.1063/1.115523

[18] Poortmans J, Arkhipov V. *Thin film solar cells: fabrication, characterization and applications*. Chichester, England; Hoboken, NJ: Wiley; 2007.

[19] Kim Y, Lee W, Jung DR, Kim J, Nam S, Kim H, et al. Optical and electronic properties of post-annealed ZnO:Al thin films. *Applied Physics Letters* 2010; **96**: 171902. DOI: 10.1063/1.3419859

[20] Ikuno T, Suzuki R, Kitazumi K, Takahashi N, Kato N, Higuchi K. SnS thin film solar cells with $Zn_{1-x}Mg_xO$ buffer layers. *Applied Physics Letters* 2013; **102**: 193901. DOI: 10.1063/1.4804603

[21] Vidal J, Lany S, d'Avezac M, Zunger A, Zakutayev A, Francis J, Tate J. Band-structure, optical properties, and defect physics of the photovoltaic semiconductor SnS. *Applied Physics Letters* 2012; **100**: 032104. DOI: 10.1063/1.3675880

[22] Heo J, Hock AS, Gordon RG. Low Temperature Atomic Layer Deposition of Tin Oxide. *Chemistry of Materials* 2010; **22**: 4964-4973. DOI: 10.1021/Cm1011108

[23] Sun L, Haight R, Sinsermsuksakul P, Kim SB, Park HH, Gordon RG. Band alignment of SnS/Zn(O,S) heterojunctions in SnS thin film solar cells. *Applied Physics Letters* 2013; **103**: 181904. DOI: 10.1063/1.4821433

[24] Scofield JH, Duda A, Albin D, Ballard BL, Predecki PK. Sputtered molybdenum bilayer back contact for copper indium diselenide-based polycrystalline thin-film solar-cells. *Thin Solid Films* 1995; **260**: 26-31. DOI: 10.1016/0040-6090(94)06462-8

[25] Johnson JB, Jones H, Latham BS, Parker JD, Engelken RD, Barber C. Optimization of photoconductivity in vacuum-evaporated tin sulfide thin films. *Semiconductor Science and Technology* 1999; **14**: 501-507. DOI: 10.1088/0268-1242/14/6/303

[26] Piacente V, Foglia S, Scardala P. Sublimation study of the tin sulphides SnS_2, Sn_2S_3, and SnS. *Journal of Alloys and Compounds* 1991; **177**: 1: 17-30. DOI: 10.1016/0925-8388(91)90053-X

[27] Greyson EC, Barton JE, Odom TW. Tetrahedral zinc blende tin sulfide nano and microcrystals. *Small* 2006; **2**: 3: 368-371. DOI: 10.1002/smll.200500460

[28] Avellaneda D, Nair MTS, Nair PK. Polymorphic tin sulfide thin films of zinc blende and orthorhombic structures by chemical deposition. *Journal of the Electrochemical Society* 2008; **155**: D517-D525. DOI: 10.1149/1.2917198

[29] Malone BD, Kaxiras E. Quasiparticle band structures and interface physics of SnS and GeS. *Physical Review B* 2013; **87**: 245312. DOI: 10.1103/PhysRevB.87.245312

[30] Bao W, Ichimura M. Orientation on band offsets at the CdS/Cu_2ZnSnS_4 interface. *International Journal of Photoenergy* 2012; **2012**: 619812. DOI: 10.1155/2012/619812

[31] Hudait MK, Zhu Y, Maurya D, Priya S, Patra PK, Ma AWK, Aphale A, Macwan I. Structural and band alignment properties of Al_2O_3 on epitaxial Ge grown on (100), (110), and (111)A GaAs substrates by molecular beam epitaxy. *Journal of Applied Physics* 2013; **113**: 134311. DOI: 10.1063/1.4799367

Figure Captions

Figure 1. (Color) (a) Schematic diagram of the solar-cell device stack under short-circuit conditions and (b) structural formula for the Sn precursor. SnS/Zn(O,S) band-alignment was drawn in accordance with the ultraviolet photoelectron spectroscopy (UPS) measurements from previous study by L. Sun *et al.* [23].

Figure 2. (Color) Plot of resistivity (green), hole carrier concentration (blue), and hole mobility (red) vs. annealing temperature in H_2S, for SnS films deposited at 70°C (dotted) and 120°C (solid). Resistivity and carrier concentration are plotted on a semilog scale, whereas mobility is plotted on a linear scale.

Figure 3. (Color) (a) Cross-sectional (with 12° tilt) and (b) plan-view FESEM images of as-deposited SnS grown at 70°C and 120°C, and SnS post-annealed at 400°C in H_2S.

Figure 4. (Color) (a) Current density vs. voltage (*J-V*) plots under dark (dotted) and 1 Sun illumination (solid) and (b) semilog *J-V* plots under dark for devices with the SnS layer annealed at different temperatures having Zn(O,S), S/Zn = 0.37 as the buffer layer.

Figure 5. (Color) (a, c) *J-V* characteristics under dark (dotted) and 1 Sun illumination (solid) and (b, d) semilog *J-V* characteristics under dark for devices with varied stoichiometry of the Zn(O,S) buffer layer. Comparison of the SnS layer annealed in H_2S at 300°C (a, b) and 400°C (c, d).

Figure 6. (Color) X-ray diffraction scans of the as-deposited SnS grown at 70°C and 120°C, and SnS films grown at 120°C annealed in pure H_2S at various temperatures. Vertical lines represent orthorhombic SnS (*o*-SnS), cubic SnS (*c*-SnS), and Mo diffraction peak positions listed by JCPDS No. 00-039-0354, 04-004-8426, and 00-004-0809, respectively.

Figure 7. (Color) External quantum efficiency (EQE) of the various solar cell devices.

Table Titles

Table 1. Solar cell parameters of devices with Zn(O,S), S/Zn = 0.37 as the buffer layer.

Table 2. Comparison of solar cell parameters of devices with SnS deposited at 120°C and annealed at 300°C and 400°C using different Zn(O,S) layers.

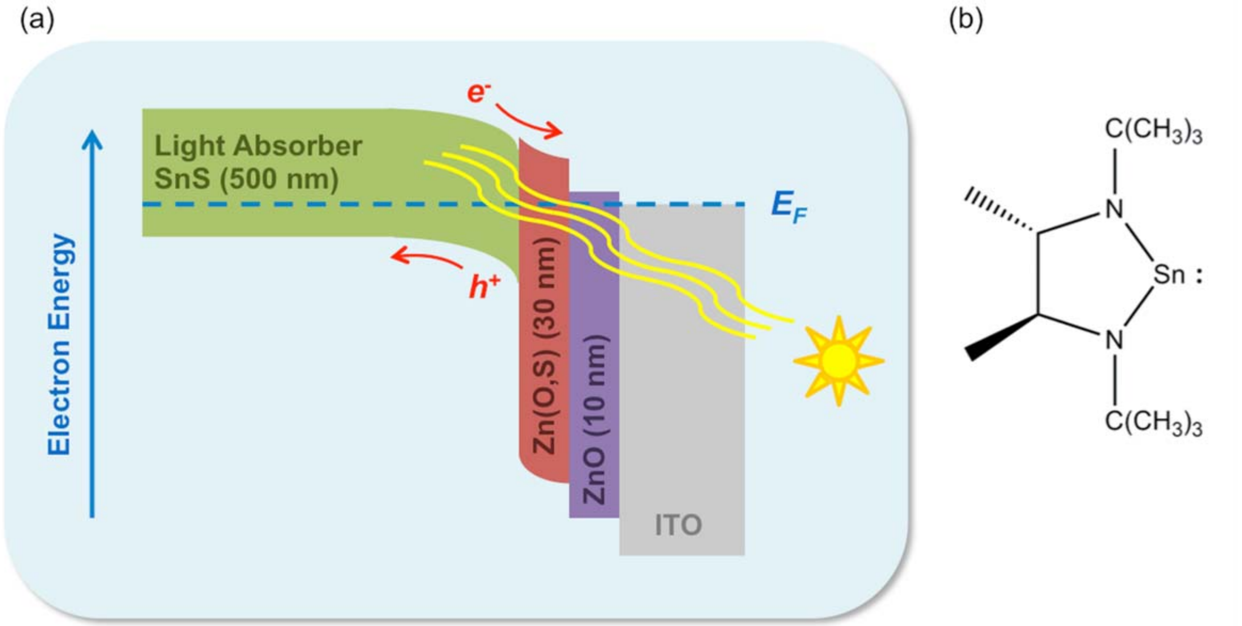

Figure 1. (Color) (a) Schematic diagram of the solar-cell device stack under short-circuit conditions and (b) structural formula for the Sn precursor. SnS/Zn(O,S) band-alignment was drawn in accordance with the ultraviolet photoelectron spectroscopy (UPS) measurements from previous study by L. Sun *et al.* [23].

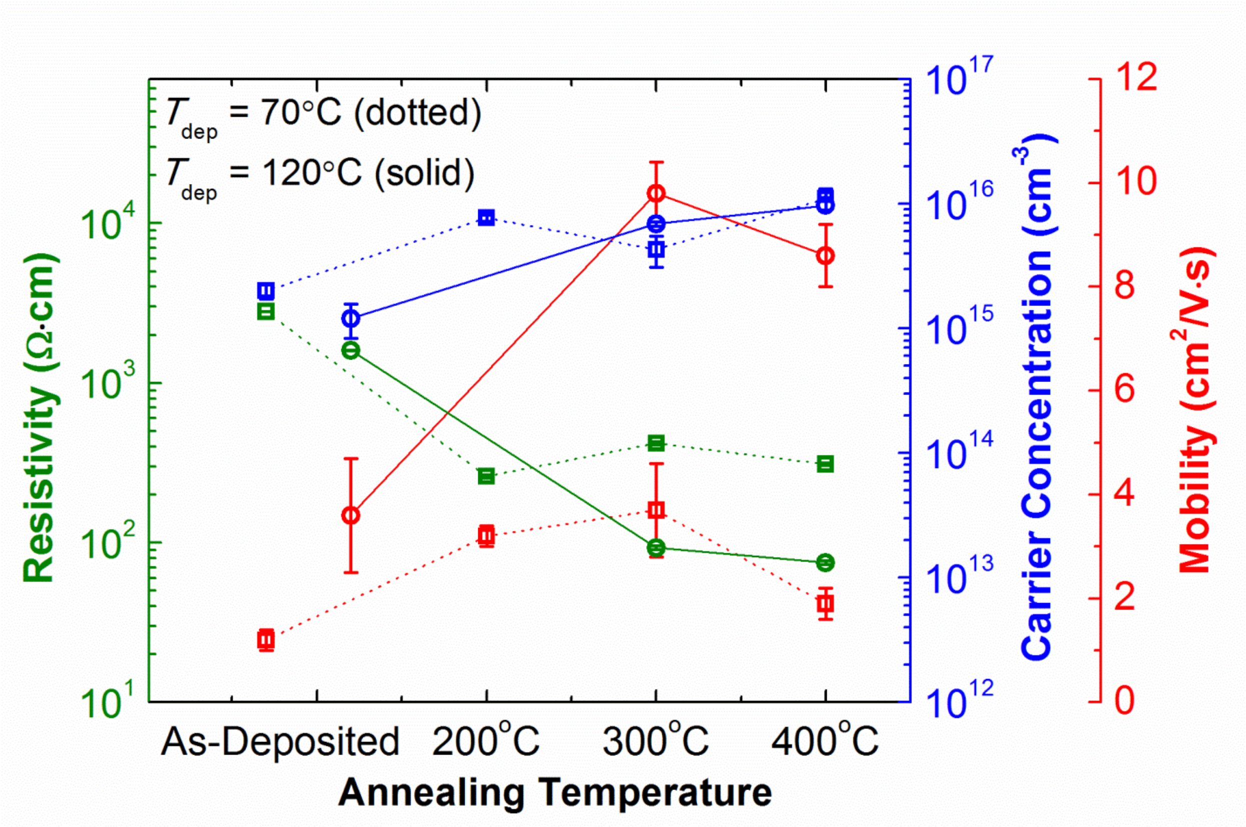

Figure 2. (Color) Plot of resistivity (green), hole carrier concentration (blue), and hole mobility (red) vs. annealing temperature in H_2S, for SnS films deposited at 70°C (dotted) and 120°C (solid). Resistivity and carrier concentration are plotted on a semilog scale, whereas mobility is plotted on a linear scale.

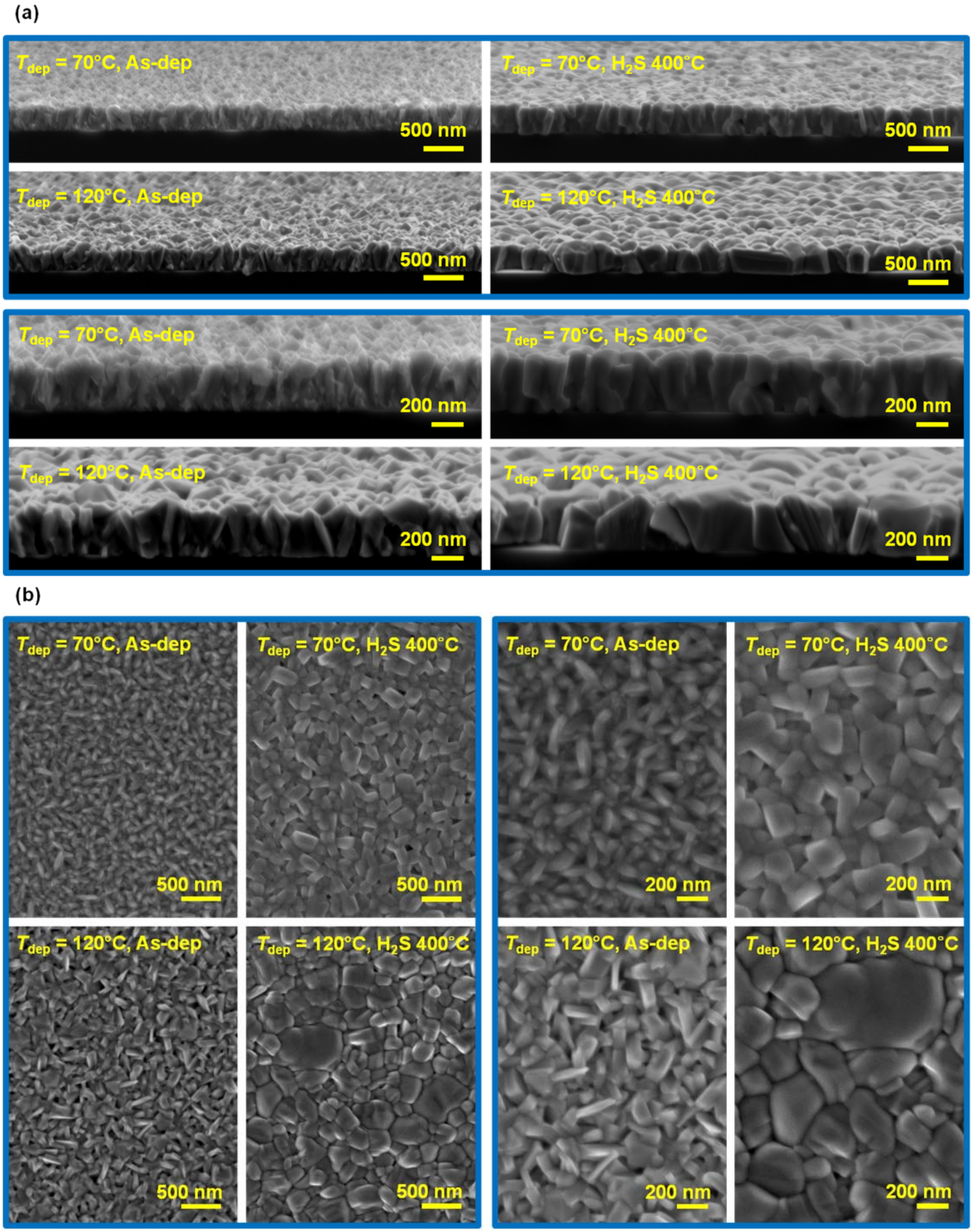

Figure 3. (Color) (a) Cross-sectional (with 12° tilt) and (b) plan-view FESEM images of as-deposited SnS grown at 70°C and 120°C, and SnS post-annealed at 400°C in H_2S.

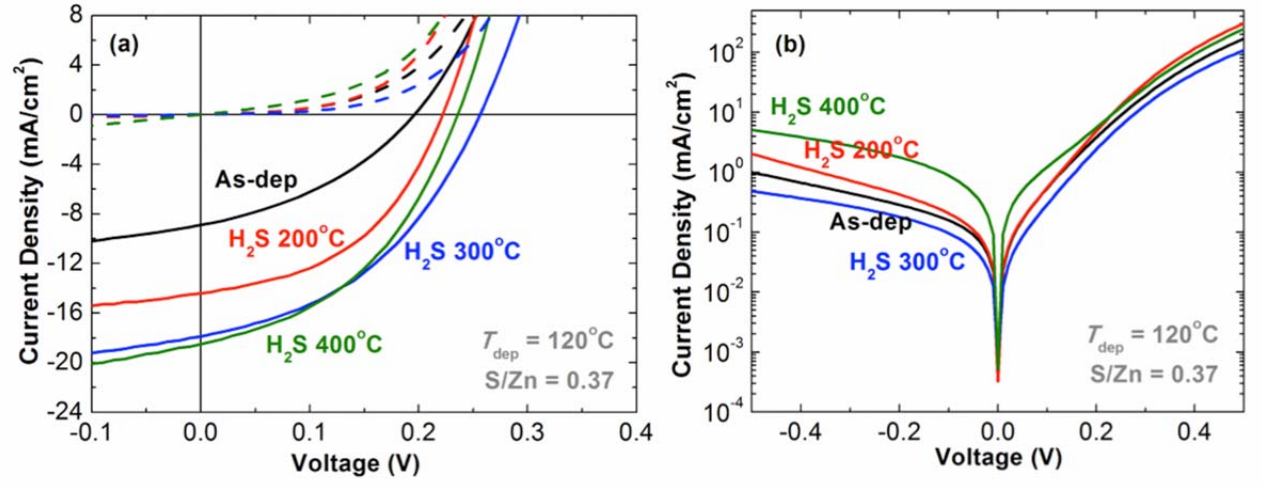

Figure 4. (Color) (a) Current density vs. voltage (*J*-*V*) plots under dark (dotted) and 1 Sun illumination (solid) and (b) semilog *J*-*V* plots under dark for devices with the SnS layer annealed at different temperatures having Zn(O,S), S/Zn = 0.37 as the buffer layer.

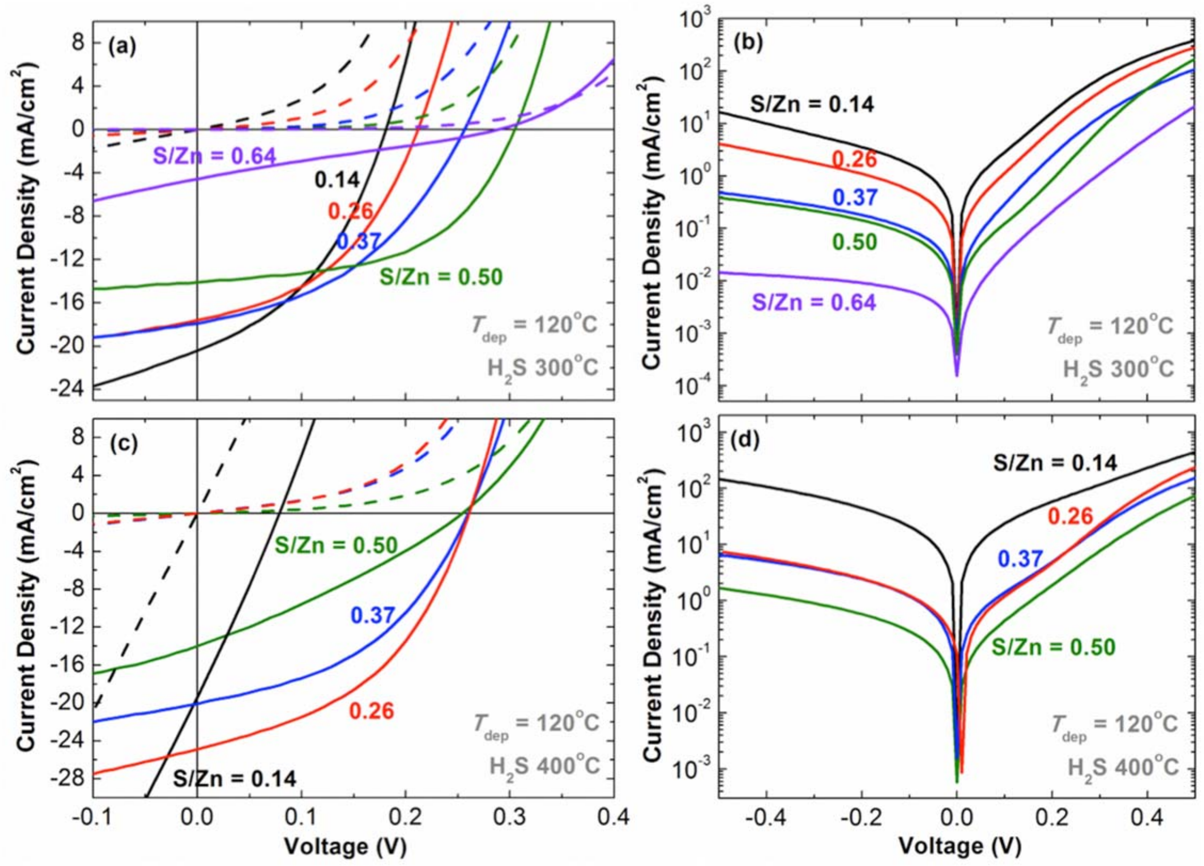

Figure 5. (Color) (a, c) *J-V* characteristics under dark (dotted) and 1 Sun illumination (solid) and (b, d) semilog *J-V* characteristics under dark for devices with varied stoichiometry of the Zn(O,S) buffer layer. Comparison of the SnS layer annealed in H_2S at 300°C (a, b) and 400°C (c, d).

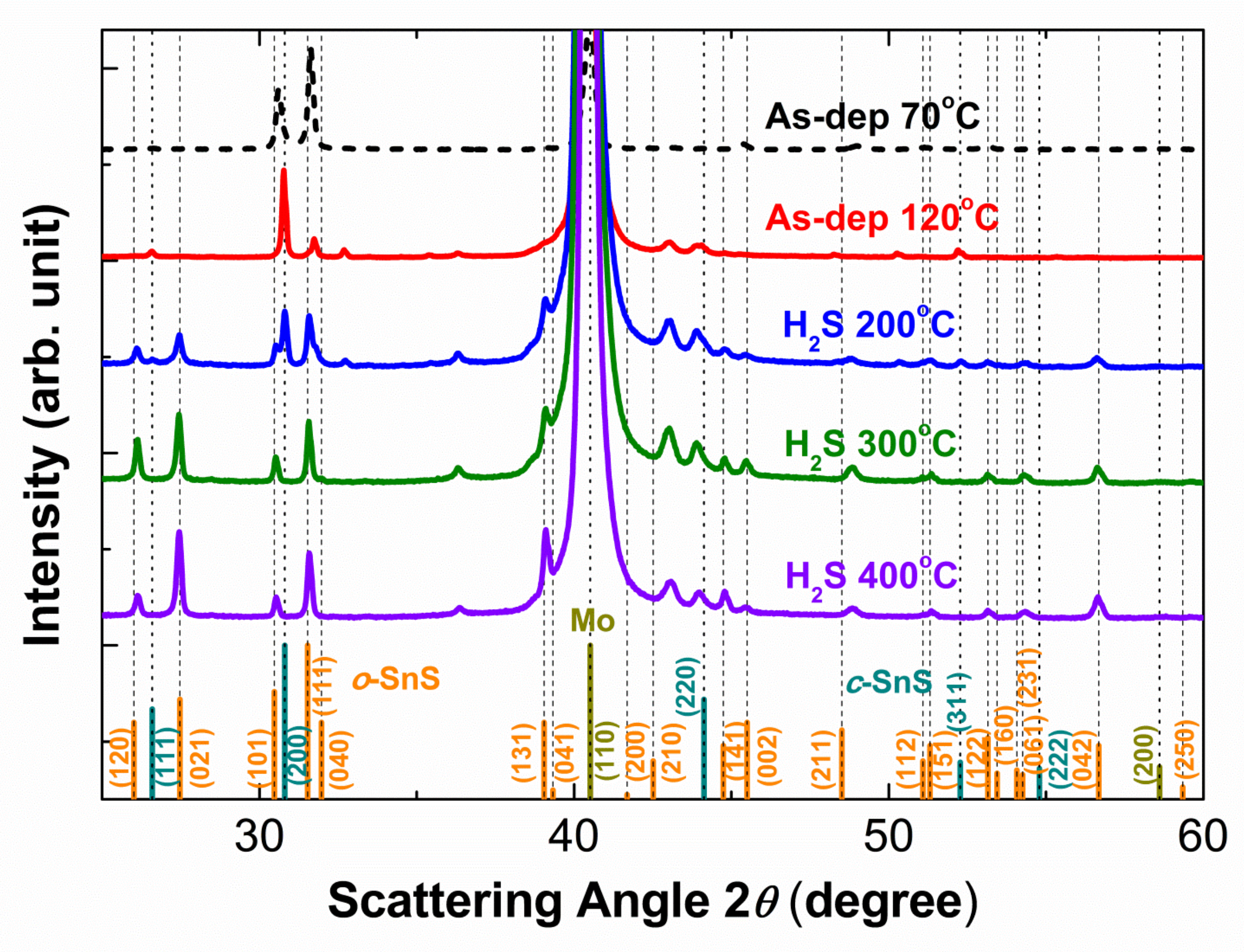

Figure 6. (Color) X-ray diffraction scans of the as-deposited SnS grown at 70°C and 120°C, and SnS films grown at 120°C annealed in pure H_2S at various temperatures. Vertical lines represent orthorhombic SnS (*o*-SnS), cubic SnS (*c*-SnS), and Mo diffraction peak positions listed by JCPDS No. 00-039-0354, 04-004-8426, and 00-004-0809, respectively.

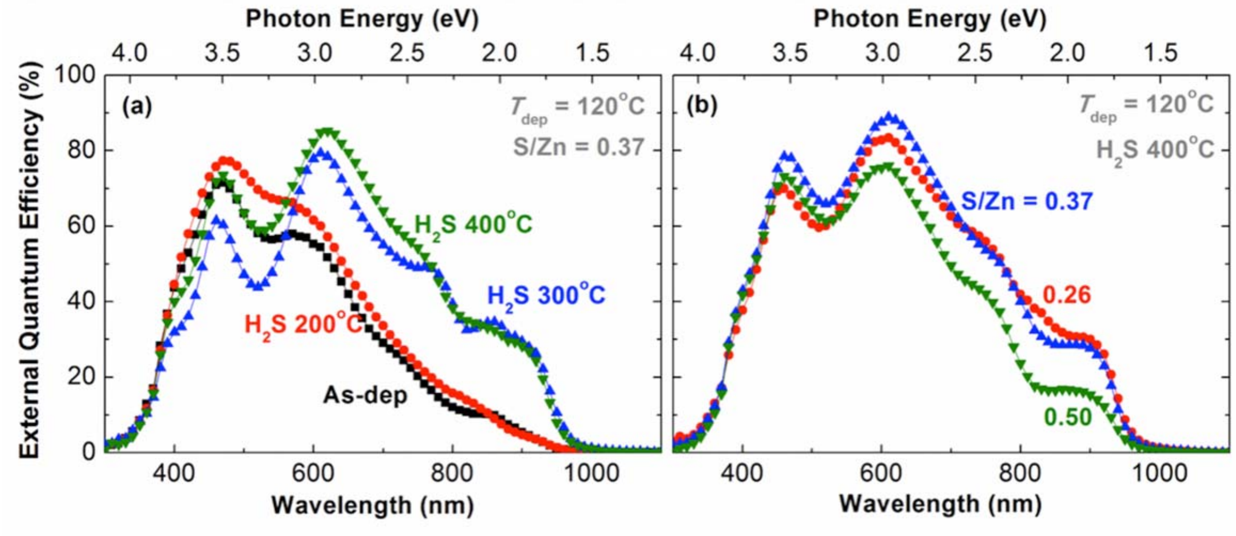

Figure 7. (Color) External quantum efficiency (EQE) of the various solar cell devices.

Table 1. Solar cell parameters of devices with Zn(O,S), S/Zn = 0.37 as the buffer layer.

SnS Annealing	J_{SC} (mA/cm^2)	V_{OC} (mV)	*FF* (%)	η (%)
As-deposited, T_{dep} = 120°C	7.8	200	36.2	0.6
H_2S 200°C	14.4	222	45.7	1.5
H_2S 300°C	17.9	256	42.0	1.9
H_2S 400°C	18.5	235	42.8	1.9

Table 2. Comparison of solar cell parameters of devices with SnS deposited at 120°C and annealed at 300°C and 400°C using different Zn(O,S) layers.

SnS Annealing	S/Zn in Zn(O,S)	J_{SC} (mA/cm^2)	V_{OC} (mV)	*FF* (%)	η (%)
H_2S 300°C	0.14	20.4	181	40.1	1.5
	0.26	17.6	212	43.7	1.6
	0.37	17.9	256	42.0	1.9
	0.50	14.1	305	53.1	2.3
	0.64	4.6	289	25.1	0.3
H_2S 400°C	0.14	19.4	79	26.4	0.4
	0.26	24.9	261	44.4	2.9
	0.37	20.1	260	43.9	2.3
	0.50	14.0	254	29.3	1.1